

A broadband X-ray spectral study of the Seyfert 1 galaxy ESO 141–G055 with *XMM-Newton* and *NuSTAR*

Ritesh Ghosh^{1*} & Sibasish Laha^{2,3†},

¹Visva-Bharati University, Santiniketan, Bolpur 731235, West Bengal, India.

²Astroparticle physics laboratory, NASA Goddard Space Flight Center, Greenbelt, MD 20771, USA.

³Center for Research and Exploration in Space Science and Technology (CREST) and Department of Physics, University of Maryland, Baltimore County, 1000 Hilltop Circle, Baltimore, MD 21250, USA

30 July 2020

ABSTRACT

We have extensively studied the broadband X-ray spectra of the source ESO 141–G055 using all available *XMM-Newton* and *NuSTAR* observations. We detect a prominent soft excess below 2 keV, a narrow Fe line and a Compton hump (> 10 keV). The origin of the soft excess is still debated. We used two models to describe the soft excess: the blurred reflection from the ionized accretion disk and the intrinsic thermal Comptonisation model. We find that both of these models explain the soft excess equally well. We confirm that we do not detect any broad Fe line in the X-ray spectra of this source, although both the physical models prefer a maximally spinning black hole scenario ($a > 0.96$). This may mean that either the broad Fe line is absent or blurred beyond detection. The Eddington rate of the source is estimated to be $\lambda_{\text{Edd}} \sim 0.31$. In the reflection model, the Compton hump has a contribution from both ionized and neutral reflection components. The neutral reflector which simultaneously describes the narrow Fe $K\alpha$ and the Compton hump has a column density of $N_{\text{H}} \geq 7 \times 10^{24} \text{cm}^{-2}$. In addition, we detect a partially covering ionized absorption with ionization parameter $\log \xi / \text{erg cm s}^{-1} = 0.1_{-0.1}^{+0.1}$ and column density $N_{\text{H}} = 20.6_{-1.0}^{+1.0} \times 10^{22} \text{cm}^{-2}$ with a covering factor of $0.21_{-0.01}^{+0.01}$.

Key words: galaxies: Seyfert, X-rays: galaxies, quasars: individual: ESO 141–G055

1 INTRODUCTION

Active Galactic Nuclei (AGNs) are centres of powerful radiation ranging from radio to Gamma rays. It is commonly believed that a supermassive black hole (SMBH) accretes matter at a very high rate and thereby emit huge radiation and particle outflows. However, the SMBHs and the central active engine of an AGN remain spatially unresolved to date in any wavelength band. It is still not clear how the accretion disk is formed and the different reprocessing media around the SMBH are structured. Broadband X-ray spectra from AGN, therefore, serves as an important tool to investigate the physics, dynamics and geometry of matter surrounding the SMBH.

The broadband X-ray continua of AGNs are dominated by a powerlaw emission that extends from soft to hard X-rays ($\sim 100 - 500$ keV). It is commonly believed to be the result of inverse Compton scattering of the seed UV photons from the accretion disk by a hot ($T \sim 10^9$ K) optically thin corona (Shakura & Sunyaev 1973; Haardt & Maraschi 1993). Although the exact geometry and

location of the corona is still debated, the powerlaw emission from it has been detected in almost all AGN. The hard X-ray coronal photons shine onto the accretion disk and other neutral and ionized media around the central engine thereby creating a reprocessed emission in X-rays, resulting in distinct spectral features.

Depending on the intensity of X-ray irradiation, the accretion disk becomes ionized and the hard X-ray photons reflected off the accretion disk produce signatures of ionized reflection in soft X-rays (e.g., Ross & Fabian 2005; García & Kallman 2010) in the X-ray spectrum. If the reflection happens near enough to the SMBH where it is blurred and distorted by relativistic effects, then we do not see individual emission lines but a continuous emission in the soft X-rays (e.g., Laor 1991; Crummy et al. 2006). In most AGNs, there has been the detection of excess emission in the soft X-rays over and above the powerlaw, popularly known as the soft X-ray excess (Singh et al. 1985), the origin of which is still unknown. The blurred ionized reflection is believed to be one of the possible mechanisms producing it, along with a broad Fe K emission line at $\sim 6.4 - 6.9$ keV. However, other models such as thermal Comptonisation has also been proposed for the possible origin of the soft X-ray excess. Despite several theoretical and observational

* Email: ritesh.ghosh1987@gmail.com,

riteshghosh.rs@visva-

bharati.ac.in

† Email: sibasish.laha@nasa.gov

studies on this matter, the origin of the soft X-ray excess is still debated.

In this work, we take a broadband spectroscopic approach to address the origin of the soft excess, the Fe K line complex and the Compton hump at $E > 10$ keV in the Seyfert 1 galaxy ESO 141–G055 (Elvis et al. 1978) where the presence of soft excess and Fe line have been affirmatively detected by previous studies (Turner et al. 1993; Gondoin et al. 2003). A recent NuSTAR observation in 2016 gives us a rare opportunity to take a hard X-ray (> 10 keV) look of this source. The spectral energy distribution is marginally variable in both optical/UV and X-ray band (Chapman et al. 1985; Winkler 1992), and hence ideal for time-averaged spectroscopic studies.

In this paper, we investigate the origin of the soft excess and the hard X-ray Compton hump consistently using broadband spectral fitting techniques, in the light of prevalent disk ionized reflection models. The main science questions we address in this work are 1. Is the disk reflection entirely responsible for both the soft and hard X-ray excess? 2. Do we detect a broad Fe emission line? and 3. what fraction of hard X-ray reflection arises from ionized reflection? The paper is organised as follows: Section 2 describes the observation and data reduction techniques. The steps taken in the spectral analysis are discussed in Section 3. Section 4 discusses the results followed by conclusions in Section 5. Throughout this paper, we assumed a cosmology with $H_0 = 71 \text{ km s}^{-1} \text{ Mpc}^{-1}$, $\Omega_\Lambda = 0.73$ and $\Omega_M = 0.27$.

2 OBSERVATION AND DATA REDUCTION

ESO 141–G055 was observed five times by *XMM-Newton* in the period from 2001 October 09 to 2007 October 30 and once by *NuSTAR* in 2016 July 15. The details of the observations and the short notation of the observation ids are listed in Table 1. The joint spectral analysis of *XMM-Newton* and *NuSTAR* provide us with a unique opportunity to study the broad energy range of 0.3–70 keV necessary for constraining neutral and disk reflection models.

We reprocessed the EPIC-pn data from *XMM-Newton* using V18.0.0 of the Science Analysis Software (SAS) with the task *epchain* and using the latest calibration database available at that time. We used EPIC-pn data because of its higher signal to noise ratio as compared to MOS. The EPIC-pn data was not available for observation taken in 2001 so we used MOS data instead and reprocessed the data with the task *emchain*. Good time intervals are selected from clean calibrated event lists by removing intervals dominated by flaring particle background in energy > 10 keV, using a rate cutoff of $< 1 \text{ cts}^{-1}$ for the pn and $< 0.35 \text{ cts}^{-1}$ for the MOS data respectively. The EVSELECT task was used to select single and double events for both the EPIC-pn (*PATTERN* ≤ 4 , *FLAG* == 0) and EPIC-MOS (*PATTERN* ≤ 12) source event lists, from a circular source region with a radius of 40 arcsec centred on the centroid of the source image. The background regions were selected with a circle of 40" located on the same CCD, but away from the source. The time-averaged source + background and background spectra, as well as the response matrix function (RMF) and auxiliary response function (ARF) for each observation, were calculated using the *xmmselect* command in SAS. All the observations were checked for possible pile up using the command *epatplot* in SAS and we found that none of them is piled up. The *XMM-Newton* spectra were grouped by a minimum of 200 counts per channel for EPIC-pn and 100 counts per channel for

the EPIC-MOS data and a maximum of three resolution elements using the command *specgroup*. The optical monitor (OM) camera permits multiwavelength observations of the source simultaneously in the X-ray and optical/UV bands. We reprocessed the OM data using the SAS task *omichain* and used only fluxes measured by the UVW2 instrument for consistency as it is the only common filter that is used in all *XMM-Newton* observations. Here we note that the peak wavelength (2120Å) is relatively nearer to 2500Å than other filter bands except that for UVM2. The observed UV fluxes were corrected for the Galactic reddening assuming Fitzpatrick (1999) reddening law with $R_v = 3.1$ and the Galactic extinction coefficient value used was 0.841.

ESO 141–G055 was observed only once by *NuSTAR* in 2016 July 15. We reprocessed the *NuSTAR* data (both FPMA and FPMB) and produced cleaned event files using the standard pipeline NUPIPELINE (V1.9.2), part of HEASOFT V6.27 package, and instrumental responses from NuSTAR CALDB version V20191219. The light curves were created using *NUPRODUCTS* command. For light curves and spectra, we used a circular extraction region of 80" and 100" for source and background respectively. The *NuSTAR* spectra were grouped by a minimum count of 200 per energy bin, using the command *grppha* in the *HEASOFT* software.

3 DATA ANALYSIS

In our work, we used a set of phenomenological models to fit the broadband spectra to identify the statistically significant spectral features and if they are variable with time. As a next step, we use physically motivated spectral models to obtain the parameter values of interest. This exercise helps to identify the features that are present in the broad-band spectra and can serve as a motivation for the use of specific physical models. We used XSPEC (Arnaud 1996) version 12.10.1, and employed a χ^2 minimization technique to fit the data sets. We quote the errors on the best-fit parameters at the 90% confidence level and used Verner cross-sections and Wilms abundances to estimate the effect of Galactic absorption for all the spectral analysis.

The simultaneous spectral fit of *XMM-Newton* and *NuSTAR* spectra was carried out with a physical set of models. The simultaneous fit helps us to constrain the physical parameters in the broad energy range. Section 3.2 discusses in detail the methods and assumptions followed during these simultaneous spectral fits. A preliminary look at the spectra of the source by fitting an absorbed powerlaw model in the 4 – 5 keV energy band and extrapolating to the rest of the X-ray band reveals a prominent soft excess (at $E < 2.0$ keV) for all *XMM-Newton* observations along with a Fe line complex at 6 – 7 keV whereas, the *NuSTAR* data revealed a hard X-ray excess above > 10 keV (See Fig. 1). The value of Galactic absorption column density ($4.9 \times 10^{20} \text{ cm}^{-2}$) is taken from Dickey & Lockman (1990). An additional emission line of unknown origin is detected at 2.5 keV for all the *XMM-Newton* observations.

3.1 The phenomenological models

The baseline phenomenological model used here consists of a neutral Galactic absorption (tbabs), a photoionized absorption model for partially ionized material (zxipcf), a multiple blackbody component to model the soft X-ray excess (diskbb, Mitsuda et al. 1984), the coronal emission described by a power

law and the *PEXRAV* model to account for the reflection component from the neutral medium. We used two Gaussian profile to describe the excess emission at around 6.4 keV and 2.5 keV. An energy-independent multiplicative factor was used to account for the relative normalization between different instruments of *XMM-Newton* and *NuSTAR*. In XSPEC notation, the phenomenological model reads as `constant × tbabs × zxcipcf × (powerlaw + diskbb + zgauss + pexrav)`. The inclusion of a partially ionized absorption model *zxcipcf*, that uses a grid of XSTAR (Kallman & Bautista 2001) photoionized absorption models (calculated assuming a microturbulent velocity of 200 km s^{-1}) significantly improved the statistics for all *XMM-Newton* observations. We did not detect intrinsic neutral absorption excess of the Galactic absorption for any of the *XMM-Newton* observations. The *XMM-Newton* energy band ($< 10 \text{ keV}$) is insufficient to constrain the *pexrav* reflection parameters. Upon using *NuSTAR* there is a statistically significant improvement (See Table 2). The phenomenological model provides a satisfactory description to the *NuSTAR* as well as *XMM-Newton* spectra (see Fig. 2). We note that an additional excess in the residual at 0.5 keV was present for xmm04 and xmm05. Addition of a Gaussian line profile to the set of phenomenological models yielded a much better fit for both these observations ($\chi^2/\text{dof} = 171/134$ and $201/147$ for xmm04 and xmm05 respectively). The best-fit parameters and the fit statistics obtained using the phenomenological models are quoted in Table 2. We also included the improvement in statistics ($\Delta\chi^2/\text{dof}$) for each spectrum on the addition of the discrete emission line models to determine the statistical significance of the model.

The Fe K_α line detected at 6.4 keV in the *NuSTAR* observation was fitted with a Gaussian which yielded an equivalent width of $98 \pm 21 \text{ eV}$. The improvement in the fit statistics is $\Delta\chi^2/\text{dof} = 113/3$, which reflects a > 99.99 per cent confidence in the detection of the emission line (Lampton et al. 1976). For *XMM-Newton* observations, a similar approach provided an equivalent-width values of $76 \pm 12 \text{ eV}$, $52 \pm 11 \text{ eV}$, $55 \pm 17 \text{ eV}$, $56 \pm 19 \text{ eV}$ and $73 \pm 19 \text{ eV}$, for xmm01, xmm02, xmm03, xmm04 and xmm05 respectively with significant improvement in the fit statistics (see Table 2). Next, we replaced the Gaussian profile with the *diskline* model (Fabian et al. 1989) to check the presence of broad Fe emission in the spectra. We did not find any significant improvement in the fit statistics ($\Delta\chi^2/\text{dof} = 7/3$) for the *NuSTAR* data. The fit worsens for *XMM-Newton* observations ($\Delta\chi^2 = 5, 9, 3, 6,$ and 7 for xmm01, xmm02, xmm03, xmm04, and xmm05, respectively) and we could not constrain model parameters e.g., the inner radius, the emissivity index and the inclination angle. These results indicate that a broad emission line is not required for any of these observations.

3.2 The physical models

The use of phenomenological models has confirmed the presence of soft and hard excess in the broad X-ray energy band. In this section, we try to simultaneously describe both soft and hard X-ray excess using two sets of physical models. The first model assumes that both the soft and the hard excess arise from a disk ionized reflection. In XSPEC notation, the first set of models reads as (`constant × tbabs × zxcipcf × (relxill + MYTorus)`). Here, *relxill* model (version 1.3.5, García et al. 2014) describes the soft X-ray excess, the power-law continuum and the reflection of primary hard X-ray photons off an ionized accretion disk while *MYTorus* (Murphy & Yaqoob 2009; Yaqoob 2012) models the cold, distant,

neutral reflection from Compton thick medium that contributes to the Compton hump. The photon index Γ in *MYTorus* and the primary power-law component of the *relxill* model were tied together. The *MYTorus* inclination angle, the equatorial column density and the normalization of the individual components, i.e., the *MYTorus line* and the *MYTorus scattered*, were left free to vary. The inclination angles of the *relxill* and *MYTorus* models were not tied as they are two entirely different reprocessing medium and were treated as separate quantities. As with phenomenological models, we have added a partially covering ionized absorption model *zxcipcf* for all the observations, to account for any ionized absorption along the line of sight. We checked for possible variation in the ionization parameter and the covering fraction of the partial absorber. The best-fit parameter values are within 3σ errors for all the observations and hence tied with each other. For all the observations, a Gaussian line profile is added to fit the emission at 2.5 keV whose origin is unknown. The *relxill* model assumes a coronal or lamp-post geometry of scattering, where the source of primary X-ray emission (corona) irradiates the accretion disk from the top and the hard X-ray photons get Compton scattered from the accretion disk. Hence, it accounts for the soft X-ray excess and the relativistic hard X-ray emission above 10 keV, contributing to the Compton hump. A broken power-law emissivity profile ($E(r) \propto r^{-q}$), is typically assumed by the *relxill* model where E is the emissivity of the gas due to reflection and q is the emissivity index. In Newtonian geometry, for a point source, the emissivity at a large radius out from the source has a form r^{-3} . In the general relativistic high-gravity regime the inner emissivity profile will depend upon the location, spatial extent and geometry of the source and calculations (Dabrowski & Lasenby 2001; Miniutti et al. 2003; Wilkins & Fabian 2011) suggest a very steeply falling profile in the inner regions of the disk. Recent studies of accretion disk/corona emission using the *relxill* model support this scenario (Ghosh et al. 2018; Tomsick et al. 2018). The *relxill* model parameter r_{br} determines this transition from relativistic geometry to Newtonian geometry. Thus in our fits, the emissivity index of the inner part of the accretion disk at $r < r_{\text{br}}$ has values ranging from $3 < q < 10$, while at the outer part of the disk at $r > r_{\text{br}}$, the index is fixed to 3.

The best-fitting model parameters along with the best-fitting statistics for *NuSTAR* and *XMM-Newton* observations are listed in Table 3. The model parameters that are unlikely to change within the human timescale were tied to each other, e.g., the black hole spin, the inclination angle, the ionization parameter of the accretion disk. The photon index Γ , the normalization flux and the reflection fraction of all the observations were made free to vary. For the *XMM-Newton* observations, the *MYTorus* parameters are not well constrained possibly due to absence of the $> 10 \text{ keV}$ spectrum and were tied with *NuSTAR* best-fit parameter values. The simultaneous analysis of all the observations with this set of physical models produced a good fit with the fit statistic $\chi^2/\text{dof} = 2314/1997$. We estimated the high energy cutoff of the primary power-law component using the *NuSTAR* observation. We found a lower limit on the high energy cutoff (E_c) to a value of $E_c > 276 \text{ keV}$. We tied this value for all other observations. We also tied the inner radius for all *XMM-Newton* observations for better constrain on the black hole spin. The broadband spectra infer the presence of a maximally spinning black hole ($a > 0.96$). The fit statistic becomes significantly poor ($\chi^2/\text{dof} = 2713/1998$) when the spin parameter is frozen to zero. We have carried out two separate fits in order to ascertain if the data prefer a maximally spinning black hole. In the first case, we kept the inner radius of the relativistic reflection model fixed to the inner circular stable orbit for a non-rotating black hole

($r_{\text{in}} = 6r_g$). In the second case, we fixed the inner radius to that of a maximally spinning black hole ($r_{\text{in}} = 1.23r_g$). We note that the broadband data prefer the maximally rotating scenario as the fit statistically worsens by $\Delta\chi^2 \sim 300$ for the non-rotating one. We get a poor ($\chi^2/\text{dof} = 2637/2000$) fit if we remove the partially covering ionized absorber model, implying that the model is statistically required by the data.

Two other flavours of *relxill* model, *relxillD* and *relxillP* have also been used to test out different reprocessing geometries. The model *relxillD* is same as *relxill* but allows a higher density for the accretion disk (between $\log N/\text{cm}^{-3} = 15$ to $\log N/\text{cm}^{-3} = 19$). The *relxillP*, on the other hand, assumes a lamp post geometry and the disk is split into multiple zones, which see a different incident spectrum due to relativistic energy shifts of the primary continuum. The use of *relxillD* and *relxillP* provided relatively poor fit compared to the *relxill* model. For *relxillD*, best-fit statistics is $\chi^2/\text{dof} = 2422/1993$ and for *relxillP*, $\chi^2/\text{dof} = 2435/1996$. The change in accretion density is not significant and found to be $\log N/\text{cm}^{-3} = 15.3^{+0.4}_{-0.5}$ for *NuSTAR* and $\log N/\text{cm}^{-3} = 16.4^{+0.6}_{-0.8}$ for *XMM-Newton* observations respectively. Interestingly, no significant variation is noticed between observations in the height of the X-ray emitting source $h \sim 3r_g$.

The second set of models we used assumes that the soft X-ray excess arises from thermal Comptonization of disk photons by a warm ($T \sim 0.5 - 1$ keV) and optically thick ($\tau \sim 10 - 20$) corona (Magdziarz et al. 1998; Done et al. 2012). The hard excess, in this case, arises exclusively due to neutral Compton reflection. The broadband model in XSPEC notation reads as (*constant* \times *tbabs* \times *zxipcf* \times (*optxagnf* + *MYTorus*)). In the model *optxagnf* (Done et al. 2012), the gravitational energy released in the accretion process serves as the power source of the disk emission in UV, the soft X-ray excess, and the power-law emission. The normalization flux of this model is determined by the black hole mass, the Eddington rate, the black hole spin and the distance. Hence the model normalization is frozen at unity. The SMBH mass used $\sim 3.98 \times 10^7 M_\odot$ was obtained from Lubiński et al. (2016), who derived it from the average values of stellar velocity dispersion. Similar to the ionized reflection model, we followed a simultaneous fitting approach with all the data sets. The black hole spin, the optical depth of the soft Comptonisation component and the coronal radius were tied between the observations. The Eddington ratio, the photon index and the parameter f_{pl} , that determines the fraction of the power below the coronal radius emitted in the hard comptonisation component, were made free to vary. The fit resulted in comparable statistics ($\chi^2/\text{dof} = 2370/1997$) as that of our first set of physical models however, we noticed some excess in the residual at ~ 0.5 keV. Addition of a Gaussian line profile to this feature provided an improved fit ($\chi^2/\text{dof} = 2335/1994$). The best-fit line energy, $0.55^{+0.02}_{-0.02}$ indicate this excess to be an OVII emission line. Table 4 lists the best-fitting parameters obtained using this model. A detailed discussion of these results is followed in the next section.

4 RESULTS AND DISCUSSION

We have investigated the broadband X-ray spectra of the Seyfert 1 galaxy ESO 141–G055 using the latest observations from *NuSTAR* and *XMM-Newton* telescopes. In our work, for the first time, we analysed all the *XMM-Newton* and *NuSTAR* observations covering a broad X-ray energy band (0.3 – 70 keV). Using physically motivated models, we carried out a detailed study investigating the

presence and origin of the observed reflection features in the source spectra. In our analysis, we find that both ionized disk reflection and intrinsic thermal Comptonisation model yielded equally acceptable statistical fits. The soft X-ray excess (0.3 – 2.0 keV), the hard (2.0 – 10.0 keV) X-ray flux and the UV monochromatic flux at UVW2 (212 nm) for the *XMM-Newton* observations does not show any significant change between observations (See Fig. 4). The 2 – 10 keV unabsorbed luminosity ($\log L_{2-10 \text{ keV}}$) of ESO 141–G055 is consistent between 2001 and 2016. The observed values are 43.92 erg s^{-1} , 43.99 erg s^{-1} , 43.95 erg s^{-1} , 43.87 erg s^{-1} , 43.96 erg s^{-1} and 43.93 erg s^{-1} for xmm01, xmm02, xmm03, xmm04, xmm05 and *NuSTAR* observation respectively. Following the equation, $\log \kappa_{\text{Lbol}} = 1.561 - 1.853 \times \alpha_{\text{OX}} + 1.226 \times \alpha_{\text{OX}}^2$, (Lusso et al. 2010; Laha et al. 2018) we estimated the average bolometric luminosity of the AGN to be $\log L_{\text{bol}} \sim 45.23 \text{ erg s}^{-1}$ by plugging in the values of OM fluxes of *XMM-Newton* observations, the values of $L_{2-10 \text{ keV}}$ and α_{OX} , where α_{OX} is the power-law slope joining the 2 keV and the 2500Å flux. For this source, a black hole mass of $\sim 3.98 \times 10^7 M_\odot$, this implies an Eddington ratio of $\lambda_{\text{Edd}} = 0.31$ which is consistent with previous estimates (Lubiński et al. 2016; Rani et al. 2019). We detected the presence of a partially ionized absorbing material with a relatively high column density $N_{\text{H}} = 20.6^{+1.0}_{-1.0} \times 10^{22} \text{ cm}^{-2}$. The ionization parameter $\log \xi/\text{erg cm s}^{-1} = 0.1^{+0.1}_{-0.1}$, and covering fraction found in our work, $0.21^{+0.01}_{-0.01}$, is consistent with Lubiński et al. (2016). Current measurements of cutoff energies of the primary power-law component, range between 50 and 300 keV (Tortosa et al. 2018; Molina et al. 2019; Ursini et al. 2019) for bright Seyfert 1 galaxies and require spectra extending well above 50 keV for better constraints. Using relativistic reflection model, we found a lower limit to the cutoff energy, $E_c > 276$ keV. Below we discuss the main results investigating the reflection features observed in this source.

4.1 The soft excess

We detected the presence of soft X-ray excess below 2 keV for all the *XMM-Newton* observations of ESO 141–G055. We investigated the broadband multi-epoch data in detail to identify its possible origin. Recent studies show that blurred ionized reflection from the accretion disk can explain the origin of soft excess in several Seyfert 1 galaxies such as Mrk 509 (García et al. 2019), 1H 0323+342 (Ghosh et al. 2018) and Mrk 478 (Waddell et al. 2019). On the other hand, the intrinsic thermal Comptonisation model can describe the soft X-ray excess better in the sources such as Ark 120 (Vaughan et al. 2004; Porquet et al. 2018), Mrk 530 (Ehler et al. 2018), HE 1143-1810 (Ursini et al. 2020) and Zw 229.015 (Tripathi et al. 2019). We note that although these two models imply two very different interpretations of the observed spectra, it is not easy to distinguish them on statistical grounds alone. However, certain model parameters exhibited extreme values in certain fits which helped in ruling the models out e.g., in the sources HE 1143-1810 (Ursini et al. 2020) and Zw 229.015 (Tripathi et al. 2019) the ionized disk reflection model was not found suitable to describe the soft excess because the iron abundance, the inclination angle and reflection fraction were too low compared to normal values expected in Seyfert 1 galaxies. On the other hand, in Mrk 478 (Waddell et al. 2019), the flux variability between data sets favoured the ionized reflection over thermal Comptonisation model.

In this study, with ESO 141–G055, We get similar fit statistics for both the models. The parameter values constrained for these models were in a range detected in typical Seyfert 1 galax-

ies (See Table 3 and Table 4). The best-fit photon index Γ of the relativistic reflection model *relxill* determines the shape of the primary continuum and ranges between 2.0 – 2.1 for all observations. The ionization parameter of the reflecting disk is $\log \xi = 2.14^{+0.02}_{-0.02} \text{ erg cm s}^{-1}$, suggesting a low to a moderately ionized disk. The inner extent of the accretion disk ($r_{\text{in}} = 3.29^{+0.22}_{-0.24} r_{\text{g}}$) and the high emissivity index of $7.25^{+0.24}_{-0.40}$ implies that major part of the soft excess has originated from a region very close to the central supermassive black hole. The inner radius and the black hole spin are degenerate in the *relxill* model and while fitting the soft excess with this model we obtained a maximally rotating black hole ($a > 0.96$). The fit worsens statistically if we freeze the spin to zero ($\Delta\chi^2 \sim 300$). The maximally spinning black hole scenario has also been detected in previous studies in other Seyfert 1 galaxies (Ghosh et al. 2016; García et al. 2019; Ghosh et al. 2018; Waddell et al. 2019). This high value of the spin is usually associated with a broad Fe K_{α} which we do not detect in any of our spectra. Hence, we presume that the high spin we obtained may be a necessity of the model to explain the soft excess, while in reality, the spin may not be that high. The reflection fraction (R) is defined as the ratio of photons from the hot corona striking the disk with that of the photons emitted from the hot corona escaping to infinity. We obtained a relatively low but well-constrained value of R ranging between $0.35^{+0.01}_{-0.01}$ to $0.54^{+0.01}_{-0.01}$. These results imply that despite the presence of a compact corona at or above the supermassive black hole, only a small amount of primary flux illuminates the accretion disk while most of it escaping to infinity. This also explains the low to moderate ionization state of the disk. These relatively lower values are consistent with the 2001 XMM-Newton observation (Gondoin et al. 2003) and other Seyfert 1s as well, e.g., Zw 229.015, where these values are $\log \xi = 2.56^{+0.15}_{-0.15} \text{ erg cm s}^{-1}$ and $R \sim 0.4$. The iron abundance of the material in the accretion disk and the inclination of the disk to the line of sight plays an important role in describing the reflected spectra of Seyfert 1 galaxies (Crummy et al. 2006; García et al. 2014). In our study, the iron abundance when made free was consistent with solar values ($1.04^{+0.17}_{-0.07}$) and hence was fixed to 1 for all observations. We were able to constrain the inclination angle to 10^{+2}_{-1} degree which is consistent with Seyfert type 1 classification criteria.

The *optxagnf* model provides a good fit to the soft excess. This model describes the soft excess as Comptonization of thermal disk photons by a warm and optically thick corona. This warm corona could be the upper layer of the accretion disk covering roughly $10 - 20r_{\text{g}}$ of the inner region (Petrucci et al. 2013). In the source ESO 141–G055, the best-fit temperature of the warm corona varies between $T \sim 0.1 - 0.3 \text{ keV}$ and we could put a lower limit on the opacity ($\tau > 6$), implying an optically thick medium. The measured warm-corona radius (r_{corona}) is $9.09^{+0.01}_{-0.01} r_{\text{g}}$. The black hole spin inferred by the *optxagnf* model is $a > 0.98$ which is consistent with that of the *relxill* model. The fit statistically worsens (by $\Delta\chi^2 \sim 250$) if we freeze the spin to zero. We think that the spin measurement is real but the absence of any broad Fe line prevents us from making any strong claim on the spin of the black hole. We note that similar results have been previously found by Waddell et al. (2019) in other Seyfert 1s where narrow Fe line is detected. In addition, we required an OVII emission line in this fit which indicates ionized emission from the disk. Our analysis of the XMM-Newton data with *optxagnf* model shows no significant variation in the Eddington ratio from 2001 to 2006 and is consistent with $\lambda_{\text{Edd}} \sim 0.14$. This sub-Eddington rate is common among several Seyfert 1s. The accretion rate in *optxagnf* is also determined by the outer accretion flow beyond r_{corona} that contributes primarily

in the optical/UV band. Due to the absence of simultaneous optical/UV data, we could not properly constrain the λ_{Edd} value in this spectral fit with the *optxagnf* model. The fraction of power below the coronal radius emitted in the hard comptonisation component is consistent with a high value of ~ 0.9 . This implies around 90 per cent of the gravitational energy released below $9r_{\text{g}}$, is emitted as the primary X-ray emission with a photon index ~ 2.1 and the rest would contribute to the soft excess.

4.2 The Fe line complex and the Compton hump

All the spectra of ESO 141–G055 show the presence of narrow Fe emission line at $\sim 6.4 \text{ keV}$ and we did not find any signature of broad Fe line in any of the observations. The centroid energy of the Fe emission line indicates that the iron is neutral or in low ionization state, consistent with the ionization parameter of the disk reflector ($\log \xi \leq 2.14 \text{ erg cm s}^{-1}$). The use of *diskline* model did not improve the fit statistics for either NuSTAR or the XMM-Newton data. We note that although the broadband spectra of ESO 141–G055 favours the maximally rotating black hole scenario, we did not find any evidence of a broad Fe emission line. This may mean that either the broad Fe line is absent or blurred beyond detection.

The narrow Fe K_{α} emission line detected at $\sim 6.4 \text{ keV}$ has an equivalent width of $55 - 70 \text{ eV}$, typical of nearby Seyfert galaxies (Nandra et al. 1989; Pounds et al. 1989; Fukazawa et al. 2011; Ricci et al. 2014a). This narrow emission line is believed to arise when hard X-ray photons from the corona are reflected from high-column-density of neutral or lowly ionized material in the outer part of the disk and possibly the torus. The neutral reflection model *PEXRAV* and *MYTorus* can describe the Fe K emission lines consistently with the reflected continuum. Recent multiwavelength studies (Shu et al. 2011; Ricci et al. 2014b) of the narrow Fe K_{α} revealed that the line originates from a distant region ($\sim 3 \times 10^4 r_{\text{g}}$). Fukazawa et al. (2011) found a strong correlation between the equivalent width of the neutral Fe K_{α} emission line and the neutral absorption column density in the range $10^{23} - 10^{25} \text{ cm}^{-2}$. In ESO 141–G055, the *MYTorus* model yielded a good description of the narrow emission line and the Compton hump (peaking at $\sim 20 \text{ keV}$). The best-fit value of the reflection column density is found to be $\geq 7 \times 10^{24} \text{ cm}^{-2}$, suggesting a Compton thick reflection. This result favours the fact that the neutral Fe K_{α} line emission of ESO 141–G055 originates from the Compton-thick torus. We note that in ionized reflection model, the Compton hump has a contribution from distant neutral reflection from the torus. From Fig. 3, we find that in the thermal comptonization model, neutral reflection alone can provide a good description of the Compton hump. With the current data quality in NuSTAR, we can not distinguish between these two models and hence unable to efficiently isolate the contributions of the ionized and neutral reflection components which describes the Compton hump. Further deep observations of these sources are required to accomplish that.

5 CONCLUSIONS

We have extensively studied the broadband X-ray spectra of the local Seyfert 1 galaxy ESO 141–G055, investigating the presence and origin of the reflection features with a physically motivated set of models using NuSTAR and XMM-Newton data. We list the main conclusions below.

- The X-ray spectra of ESO 141–G055 is typical of local Seyfert galaxies, with the powerlaw photon index varying between $\Gamma =$

2.0 – 2.1, a prominent soft-excess, a narrow Fe line emission at ~ 6.4 keV, and a hard X-ray excess above 10 keV. Using reflection model *relxill*, we found a lower limit to the cutoff energy of the primary power-law component, $E_c > 276$ keV.

- The soft X-ray excess is equally well described by both the models: the blurred reflection from ionized disk and the intrinsic thermal comptonization of disk photons. Both these models require a maximally spinning black hole to describe the soft excess.

- We found the presence of a narrow Fe emission line at ~ 6.4 keV with an equivalent width of 55 – 70 eV, that is typical of nearby Seyfert galaxies. The best-fitting reflection column density of the *MYTorus* model is found to be $\geq 0.52 \times 10^{24} \text{ cm}^{-2}$ which indicates that the neutral Fe K_α emission line of ESO 141–G055 has originated from neutral Compton thick reflector (possibly the torus).

- The cold, distant neutral reflection from torus is a major contributor to the Compton hump along with the ionized reflection.

- We detected a partially covering ionized absorption with ionization parameter $\log \xi / \text{erg cm s}^{-1} = 0.1_{-0.1}^{+0.1}$, and a covering factor of $0.21_{-0.01}^{+0.01}$. The column density is found to be $N_{\text{H}} = 20.6_{-1.0}^{+1.0} \times 10^{22} \text{ cm}^{-2}$.

6 ACKNOWLEDGEMENTS

The authors are grateful to the anonymous referee for insightful comments which improved the quality of the paper. RG acknowledges the financial support from Visva-Bharati University and IUCAA visitor programme.

7 DATA AVAILABILITY

This research has made use of archival data of *NuSTAR* and *XMM-Newton* observatories through the High Energy Astrophysics Science Archive Research Center Online Service, provided by the NASA Goddard Space Flight Center.

REFERENCES

Arnaud k. a., 1996, in jacoby g. h., barnes j., eds, astronomical society of the pacific conference series Vol. 101, astronomical data analysis software and systems v. p. 17

Chapman G. N. F., Geller M. J., Huchra J. P., 1985, *ApJ*, **297**, 151

Crummy J., Fabian A. C., Gallo L., Ross R. R., 2006, *MNRAS*, **365**, 1067

Dabrowski Y., Lasenby A. N., 2001, *MNRAS*, **321**, 605

Dickey J. M., Lockman F. J., 1990, *ARA&A*, **28**, 215

Done c., davis s. w., jin c., blaes o., ward m., 2012, *MNRAS*, **420**, 1848

Ehler H. J. S., Gonzalez A. G., Gallo L. C., 2018, *MNRAS*, **478**, 4214

Elvis M., Maccacaro T., Wilson A. S., Ward M. J., Penston M. V., Fosbury R. A. E., Perola G. C., 1978, *MNRAS*, **183**, 129

Fabian A. C., Rees M. J., Stella L., White N. E., 1989, *MNRAS*, **238**, 729

Fitzpatrick E. L., 1999, *PASP*, **111**, 63

Fukazawa Y., et al., 2011, *ApJ*, **727**, 19

García J., Kallman T. R., 2010, *ApJ*, **718**, 695

García J., et al., 2014, *ApJ*, **782**, 76

García J. A., et al., 2019, *ApJ*, **871**, 88

Ghosh R., Dewangan G. C., Raychaudhuri B., 2016, *MNRAS*, **456**, 554

Ghosh R., Dewangan G. C., Mallick L., Raychaudhuri B., 2018, *MNRAS*, **479**, 2464

Gondoin P., Orr A., Lumb D., 2003, *A&A*, **398**, 967

Haardt F., Maraschi L., 1993, *ApJ*, **413**, 507

Kallman T., Bautista M., 2001, *ApJS*, **133**, 221

Laha S., Ghosh R., Guainazzi M., Markowitz A. G., 2018, *MNRAS*, **480**, 1522

Lampton M., Margon B., Bowyer S., 1976, *ApJ*, **208**, 177

Laor A., 1991, *ApJ*, **376**, 90

Lubiński P., et al., 2016, *MNRAS*, **458**, 2454

Lusso E., Comastri A., Vignali C., Zamorani G., Brusa M., 2010, *A&A*, **512**, A34

Magdziarz P., Blaes O. M., Zdziarski A. A., Johnson W. N., Smith D. A., 1998, *MNRAS*, **301**, 179

Miniutti G., Fabian A. C., Goyder R., Lasenby A. N., 2003, *MNRAS*, **344**, L22

Mitsuda K., et al., 1984, *PASJ*, **36**, 741

Molina M., Malizia A., Bassani L., Ursini F., Bazzano A., Ubertini P., 2019, *MNRAS*, **484**, 2735

Murphy K. D., Yaqoob T., 2009, *MNRAS*, **397**, 1549

Nandra K., Pounds K. A., Stewart G. C., Fabian A. C., Rees M. J., 1989, *MNRAS*, **236**, 39P

Petrucci P. O., et al., 2013, *A&A*, **549**, A73

Porquet D., et al., 2018, *A&A*, **609**, A42

Pounds K. A., Nandra K., Stewart G. C., Leighly K., 1989, *MNRAS*, **240**, 769

Rani P., Stalin C. S., Goswami K. D., 2019, *MNRAS*, **484**, 5113

Ricci C., Ueda Y., Paltani S., Ichikawa K., Gandhi P., Awaki H., 2014a, *MNRAS*, **441**, 3622

Ricci C., Ueda Y., Ichikawa K., Paltani S., Boissay R., Gandhi P., Stalevski M., Awaki H., 2014b, *A&A*, **567**, A142

Ross R. R., Fabian A. C., 2005, *MNRAS*, **358**, 211

Shakura N. I., Sunyaev R. A., 1973, *A&A*, **24**, 337

Shu X. W., Yaqoob T., Wang J. X., 2011, *ApJ*, **738**, 147

Singh K. P., Garmire G. P., Nousek J., 1985, *ApJ*, **297**, 633

Tomsick J. A., et al., 2018, *ApJ*, **855**, 3

Tortosa A., et al., 2018, *MNRAS*, **473**, 3104

Tripathi S., Waddell S. G. H., Gallo L. C., Welsh W. F., Chiang C. Y., 2019, *MNRAS*, **488**, 4831

Turner T. J., George I. M., Mushotzky R. F., 1993, *ApJ*, **412**, 72

Ursini F., Bassani L., Malizia A., Bazzano A., Bird A. J., Stephen J. B., Ubertini P., 2019, *A&A*, **629**, A54

Ursini F., et al., 2020, *A&A*, **634**, A92

Vaughan S., Fabian A. C., Ballantyne D. R., De Rosa A., Piro L., Matt G., 2004, *MNRAS*, **351**, 193

Waddell S. G. H., Gallo L. C., Gonzalez A. G., Tripathi S., Zoghbi A., 2019, *MNRAS*, **489**, 5398

Wilkins D. R., Fabian A. C., 2011, *MNRAS*, **414**, 1269

Winkler H., 1992, *MNRAS*, **257**, 677

Yaqoob T., 2012, *MNRAS*, **423**, 3360

Table 1. The X-ray observations of ESO 141–G055.

X-ray Satellite	observation id	Short id	Date of obs	Net exposure
<i>XMM-Newton</i>	0101040501	xmm01	09-10-2001	55 ks
	0503750301	xmm02	09-10-2007	31 ks
	0503750401	xmm03	11-10-2007	27 ks
	0503750501	xmm04	12-10-2007	76 ks
	0503750101	xmm05	30-10-2007	80 ks
<i>NuSTAR</i>	60201042002		15-07-2016	93 ks

Table 2. The best fit parameters of the baseline phenomenological models for the *NuSTAR* and *XMM-Newton* observations of ESO 141–G055.

Models	Parameter	NuSTAR	xmm01	xmm02	xmm03	xmm04	xmm05
Gal. abs.	$N_{\text{H}} (\times 10^{20} \text{ cm}^{-2})$	4.94 (f)	4.94 (f)	4.94 (f)	4.94 (f)	4.94 (f)	4.94 (f)
zxcipcf	$N_{\text{H}} (\times 10^{22} \text{ cm}^{-2})$	—	$0.39^{+0.14}_{-0.12}$	$0.84^{+0.29}_{-0.35}$	$0.64^{+0.21}_{-0.47}$	$0.29^{+0.14}_{-0.18}$	$0.38^{+0.34}_{-0.32}$
	$\log \xi$	—	$-0.5^{+0.2}_{-0.8}$	$-0.4^{+0.6}_{-0.3}$	$-0.5^{+0.2}_{-0.6}$	$-0.4^{+0.2}_{-0.1}$	$-0.2^{+0.3}_{-0.2}$
	f	—	$0.5^{+0.1}_{-0.1}$	$0.6^{+0.1}_{-0.3}$	$0.5^{+0.2}_{-0.2}$	$0.5^{+0.1}_{-0.2}$	$0.3^{+0.2}_{-0.1}$
powerlaw	Γ	$1.93^{+0.03}_{-0.03}$	$1.87^{+0.05}_{-0.03}$	$1.83^{+0.07}_{-0.09}$	$1.95^{+0.14}_{-0.14}$	$2.16^{+0.06}_{-0.06}$	$1.79^{+0.03}_{-0.04}$
	norm (10^{-3})	$8.56^{+0.04}_{-0.03}$	$7.93^{+0.67}_{-0.37}$	$7.81^{+1.09}_{-1.19}$	$7.64^{+1.21}_{-1.15}$	$8.92^{+0.45}_{-0.53}$	$6.95^{+0.40}_{-0.47}$
diskbb	T_{in} (keV)	—	$0.04^{+0.02}_{-0.01}$	$0.06^{+0.01}_{-0.01}$	$0.09^{+0.03}_{-0.03}$	$0.04^{+0.02}_{-0.02}$	$0.10^{+0.02}_{-0.03}$
	norm (10^4)	—	$9.27^{+2.85}_{-1.44}$	$9.86^{+5.51}_{-1.63}$	$1.80^{+3.73}_{-1.31}$	$8.91^{+4.29}_{-2.26}$	$0.89^{+0.81}_{-0.31}$
diskbb	T_{in} (keV)	—	$0.19^{+0.03}_{-0.01}$	$0.24^{+0.03}_{-0.03}$	$0.26^{+0.02}_{-0.02}$	$0.17^{+0.03}_{-0.01}$	$0.30^{+0.02}_{-0.03}$
	norm (10^3)	—	$1.01^{+0.49}_{-0.67}$	$0.79^{+1.13}_{-6.56}$	$0.34^{+0.55}_{-0.28}$	$1.27^{+0.56}_{-0.71}$	$0.78^{+0.13}_{-0.07}$
Gaussian	E (keV)	$6.39^{+0.09}_{-0.09}$	$6.62^{+0.15}_{-0.15}$	$6.33^{+0.07}_{-0.08}$	$6.33^{+0.05}_{-0.05}$	$6.35^{+0.05}_{-0.05}$	$6.43^{+0.07}_{-0.07}$
	σ (keV)	$0.31^{+0.11}_{-0.12}$	$0.35^{+0.20}_{-0.11}$	< 0.18	< 0.14	< 0.10	$0.12^{+0.09}_{-0.09}$
	norm (10^{-5})	$3.38^{+0.70}_{-0.71}$	$4.51^{+1.60}_{-1.96}$	$1.54^{+0.76}_{-0.70}$	$1.50^{+0.72}_{-0.64}$	$1.34^{+0.60}_{-0.51}$	$1.81^{+0.61}_{-0.47}$
	^A $\Delta\chi^2/\text{dof}$	113/3	28/3	35/3	50/3	57/3	62/3
Pexrav ^B	R	$-0.39^{+0.08}_{-0.16}$	–0.2*	–1.9*	$-1.07^{+0.85}_{-1.10}$	$-1.68^{+0.57}_{-0.65}$	> –0.22
	Incl	10*	10*	10*	10*	10*	10*
	^A $\Delta\chi^2/\text{dof}$	97/2	–	–	27/2	13/2	–
Gaussian	EqW (eV)	98	76	52	55	56	73
χ^2/dof		1334/1284	158/161	142/141	166/137	171/134	201/147

^A The $\Delta\chi^2$ improvement in statistics upon addition of the corresponding discrete component.

^B The model *pexrav* was used only for *NuSTAR* observation as it had broad band spectra necessary for constraining the parameters. The values quoted for the *XMM-Newton* observations are from the simultaneous fit of all the data sets.

(*) indicates parameters are not constrained

Table 3. Best fit parameters for observations of ESO 141–G055 with the first set of physical models. In XSPEC, the models read as (*constant* × *tbabs* × *zxipcf* × (*relxill* + *MYTorus*)).

Component	parameter	<i>NuSTAR</i>	xmm01	xmm02	xmm03	xmm04	xmm05
Gal. abs.	$N_{\text{H}}(10^{20} \text{ cm}^{-2})$	4.94 (f)					
zxipcf	$N_{\text{H}}(\times 10^{22} \text{ cm}^{-2})$	20.6 (t)	20.6 (t)	$20.6_{-1.0}^{+1.0}$	20.6(t)	20.6(t)	20.6(t)
	$\log \xi(\text{ erg s}^{-1})$	0.1(t)	0.1(t)	$0.1_{-0.1}^{+0.1}$	0.1(t)	0.1(t)	0.1(t)
	Cv_{frac}	0.21(t)	0.21(t)	$0.21_{-0.01}^{+0.01}$	0.21(t)	0.21(t)	0.21(t)
<i>relxill</i>	A_{Fe}	1(f)	1(f)	1(f)	1(f)	1(f)	1(f)
	$\log \xi(\text{ erg cm s}^{-1})$	$2.14_{-0.02}^{+0.02}$	2.14 (t)				
	Γ	$2.03_{-0.01}^{+0.01}$	$1.97_{-0.01}^{+0.01}$	$2.07_{-0.01}^{+0.01}$	$2.08_{-0.01}^{+0.01}$	$2.14_{-0.01}^{+0.01}$	$2.07_{-0.01}^{+0.01}$
	$E_{\text{cut}}(\text{ keV})$	> 276	301(t)	301(t)	301 (t)	301(t)	301(t)
	$n_{\text{rel}}(10^{-5})^a$	$18.11_{-0.05}^{+0.09}$	$14.48_{-0.22}^{+0.21}$	$21.01_{-2.89}^{+0.06}$	$19.24_{-2.65}^{+0.05}$	$15.62_{-0.05}^{+0.05}$	$19.66_{-2.70}^{+0.02}$
	q_1	$7.25_{-0.12}^{+0.11}$	$7.25_{-0.40}^{+0.24}$	7.25(t)	7.25(t)	7.25(t)	7.25(t)
	a	> 0.96	0.99(t)	0.99(t)	0.99 (t)	0.99(t)	0.99(t)
	$R(\text{reflfrac})$	$0.10_{-0.01}^{+0.01}$	$0.47_{-0.05}^{+0.05}$	$0.35_{-0.01}^{+0.01}$	$0.35_{-0.01}^{+0.01}$	$0.54_{-0.01}^{+0.01}$	$0.35_{-0.01}^{+0.01}$
	$R_{\text{in}}(r_g)$	$3.06_{-0.03}^{+0.03}$	$3.29_{-0.24}^{+0.22}$	3.06(t)	3.06(t)	3.06(t)	3.06(t)
	$R_{\text{br}}(r_g)$	$7.2_{-0.3}^{+0.3}$	$7.1_{-0.4}^{+0.4}$	7.1(t)	7.1(t)	7.1(t)	7.1(t)
	$R_{\text{out}}(r_g)$	400 (f)	400(f)	400(f)	400(f)	400(f)	400(f)
	$i(\text{degree})$	10_{-1}^{+2}	10(t)	10(t)	10(t)	10(t)	10(t)
	<i>MYTorusL</i>	$i(\text{degree})$	> 45	57(t)	57(t)	57(t)	57(t)
norm (10^{-3})		$17.95_{-2.03}^{+2.50}$	17.95(t)	17.95(t)	17.95(t)	17.95(t)	17.95(t)
<i>MYTorusS</i>	$N_{\text{H}}(10^{24} \text{ cm}^{-2})$	> 7.1	10(t)	10(t)	10(t)	10(t)	10(t)
	norm (10^{-3})	$14.20_{-0.68}^{+2.74}$	14.20(t)	14.20(t)	14.20(t)	14.20(t)	14.20(t)
	χ^2/dof	1342/1271	191/168	165/134	185/135	189/129	242/159

Notes: (f) indicates a frozen parameter. (t) indicates a tied parameter between observations.

(a) n_{rel} represent normalization for the model *relxill***Table 4.** Best fit parameters for observations of ESO 141–G055 with the second set of physical models. In XSPEC, the models read as (*constant* × *tbabs* × *zxipcf* × (*optxagnf* + *MYTorus*)).

Component	parameter	<i>NuSTAR</i>	xmm01	xmm02	xmm03	xmm04	xmm05
Gal. abs.	$N_{\text{H}}(10^{20} \text{ cm}^{-2})$	4.94 (f)	4.94 (f)	4.94 (f)	4.94 (f)	4.94 (f)	4.94 (f)
zxipcf	$N_{\text{H}}(\times 10^{22} \text{ cm}^{-2})$	13.8(t)	13.8(t)	$13.8_{-2.0}^{+2.1}$	13.8(t)	13.8(t)	13.8(t)
	$\log \xi(\text{ erg s}^{-1})$	-0.2(t)	-0.2(t)	$-0.2_{-0.2}^{+0.2}$	-0.2(t)	-0.2(t)	-0.2(t)
	Cv_{frac}	0.28(t)	0.28(t)	$0.28_{-0.02}^{+0.02}$	0.28(t)	0.28(t)	0.28(t)
optxagnf	M_{BH}^a	3.98(f)	3.98(f)	3.98(f)	3.98(f)	3.98(f)	3.98(f)
	$d(\text{Mpc})$	163(f)	163(f)	163(f)	163(f)	163(f)	163(f)
	$(\frac{L}{L_E})$	$0.42_{-0.06}^{+0.01}$	$0.13_{-0.02}^{+0.04}$	$0.15_{-0.02}^{+0.03}$	$0.14_{-0.01}^{+0.04}$	$0.12_{-0.02}^{+0.03}$	$0.14_{-0.03}^{+0.04}$
	$kT_e(\text{ keV})$	0.08(t)	$0.26_{-0.02}^{+0.02}$	$0.08_{-0.01}^{+0.01}$	0.08(t)	0.08(t)	0.08(t)
	τ	15(t)	15(t)	> 6	15(t)	15(t)	15(t)
	$r_{\text{cor}}(r_g)$	$2.9_{-0.2}^{+0.2}$	> 4.1	$9.09_{-0.01}^{+0.01}$	9.09(t)	9.09(t)	9.09(t)
	a	0.99(t)	0.99(t)	> 0.98	0.99(f)	0.99(f)	0.99(f)
	f_{pl}	$0.90_{-0.03}^{+0.04}$	$0.95_{-0.01}^{+0.01}$	$0.95_{-0.01}^{+0.01}$	$0.96_{-0.01}^{+0.01}$	$0.93_{-0.01}^{+0.01}$	$0.96_{-0.01}^{+0.01}$
	Γ	$2.11_{-0.01}^{+0.01}$	$1.93_{-0.02}^{+0.02}$	$2.08_{-0.01}^{+0.01}$	$2.09_{-0.01}^{+0.01}$	$2.13_{-0.01}^{+0.01}$	$2.08_{-0.01}^{+0.01}$
	<i>MYTorusL</i>	$i(\text{degree})$	> 51	60(t)	60(t)	60(t)	60(t)
norm (10^{-3})		$18.15_{-0.10}^{+0.02}$	18.15(t)	18.15(t)	18.15(t)	18.15(t)	18.15(t)
<i>MYTorusS</i>	$N_{\text{H}}(10^{24} \text{ cm}^{-2})$	10.0(*)	10.0(t)	10.0(t)	10.0(t)	10.0(t)	10.0(t)
	norm (10^{-3})	$30.74_{-0.01}^{+0.01}$	30.74(t)	30.74(t)	30.74(t)	30.74(t)	30.74(t)
	χ^2/dof	1349/1277	193/169	172/133	193/134	171/128	258/160

Notes: (f) indicates a frozen parameter. (t) indicates a tied parameter between different observation.

(*) indicates parameters are not constrained.

(a): in units of $10^7 M_{\odot}$;

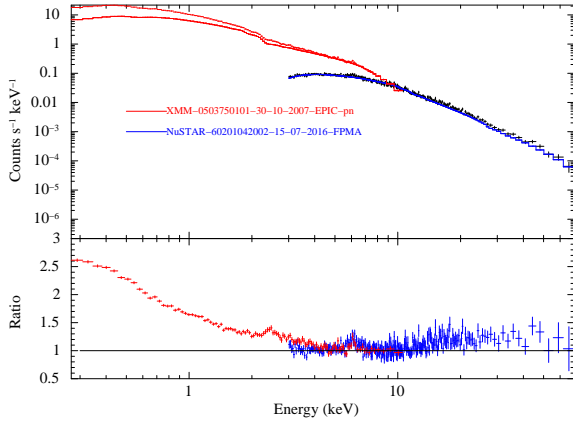


Figure 1. *Top panel:* The 0.3 – 70.0 keV joint *NuSTAR* FPMA (blue) and *xmm05* (80 ks) EPIC-pn (red) source spectra of ESO 141–G055. *Bottom panel:* The 4.0 – 5.0 keV *NuSTAR* and *XMM-Newton* spectra of ESO 141–G055 fitted with an absorbed powerlaw and the rest of the 0.3 – 70.0 keV dataset extrapolated. The broadband residuals from the fit mentioned above, showing the presence of soft X-ray excess, a Fe emission line, a hard X-ray excess (at $E > 10$ keV) and an additional excess at around 2.5 keV of unknown origin. The X-axis represents observed frame energy. The X-axis represents observed frame energy.

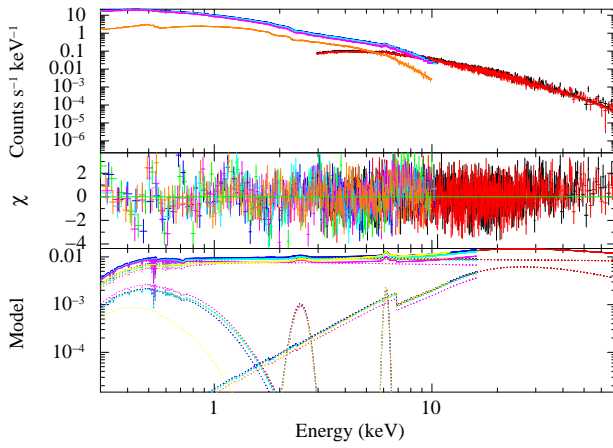


Figure 2. The 0.3 – 70.0 keV *NuSTAR* and *XMM-Newton* spectra of the source ESO 141–G055 with the best-fitting phenomenological model and residuals. The X-axis represents the observed frame energy.

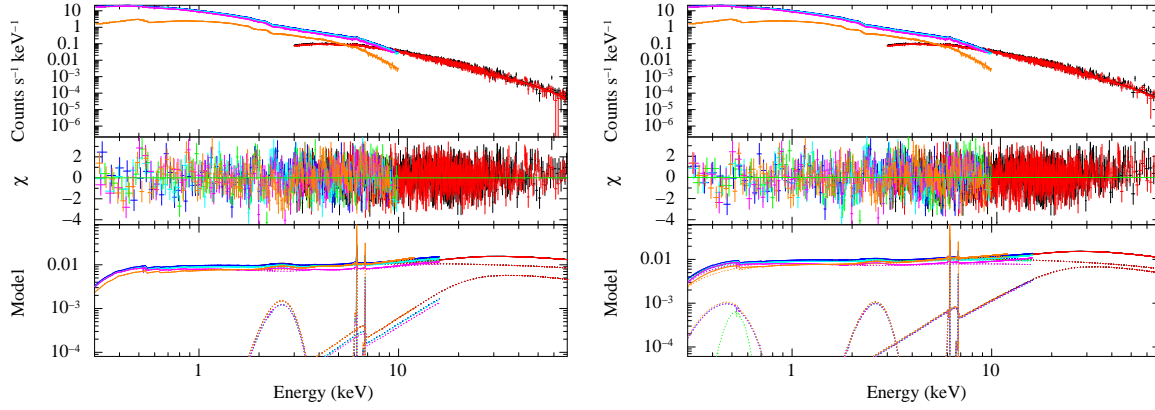


Figure 3. *Left:* The 0.3 – 70.0 keV *NuSTAR* and *XMM-Newton* spectra of the source ESO 141–G055 with the best-fitting reflection model and residuals. The *relxill* model describing simultaneously the soft X-ray excess, the broad Fe K emission line, and the relativistic reflection hump in the hard X-rays, the *MYTorus* model describing the narrow Fe K_{α} and Ni emission lines along with the Compton hump due to distant neutral reflection, are plotted in the lower panel. *Right:* Same for the Comptonization model *optxagnf*. The X-axis represents the observed frame energy.

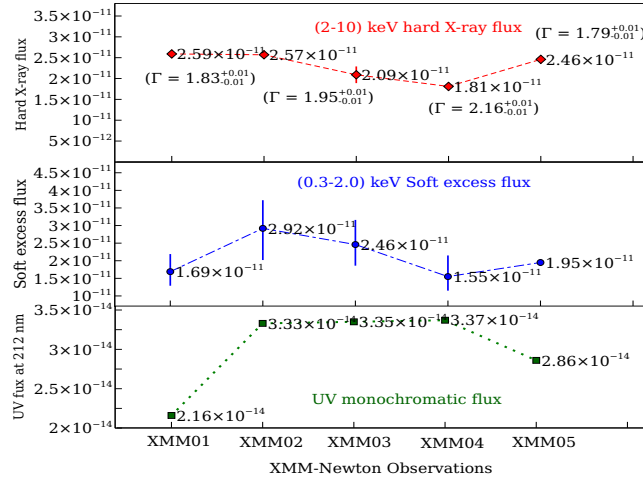


Figure 4. The soft excess (in 0.3 – 2.0 keV), the hard (2.0 – 10.0 keV) X-ray and the UV monochromatic flux (at UVW2; 212 nm) variation of five *XMM-Newton* observations of ESO 141–G055 are plotted. The measured soft excess, the 2 – 10 keV and the UV monochromatic (212nm) flux does not show any significant change between observations and are shown in circles (blue), diamonds (red) and squares (green) respectively. The X-axis represents the *XMM-Newton* observations and the Y-axis represents the measured flux in units of $\text{erg cm}^{-2} \text{s}^{-1}$.